LRP 379/89 Juin 1989

TOROIDAL EFFECTS ON CURRENT DRIVEN MODES IN TOKAMAKS

A.D. Turnbull and F. Troyon

Toroidal Effects on Current Driven Modes in Tokamaks

A.D. TURNBULL* and F. TROYON

Centre de Recherches en Physique des Plasmas
Ecole Polytechnique Fédérale de Lausanne
Av. des Bains, 21
1007 Lausanne, Switzerland

Abstract

The low β stability of a toroidal circular cross-section tokamak is reanalyzed. Although the structure of the unstable modes can be considerably modified by toroidal coupling, the overall stability picture is well represented by the so-called straight tokamak model, with the major exception that the internal kink, although stabilized by toroidal effects, still has a free-boundary counterpart — the toroidal kink mode. The toroidal kink is unstable for $q_0 < q_c \leq 1$ and is destabilized by toroidal coupling, having a growth rate γ that scales with inverse aspect ratio a/R like $\gamma \sim (a/R)^{2[q_s]}$, where $[q_s]$ is the integer part of the edge safety factor q_s.

*Present Address: General Atomics, P.O. Box 85608, San Diego, California 92138-5608, U.S.A.

1. Introduction

An understanding of the stability of tokamaks in the absence of pressure is an important ingredient in the search for the operational limits imposed by pressure-driven instabilities. In the same way, the stability of circular cross-section tokamaks needs to be well understood in order to realize the full benefits of cross-sectional shaping. The results obtained from stability studies are commonly interpreted in terms of the circular cross-section "straight tokamak" model [1–3], in which toroidicity is neglected except for its role in stabilizing the n=1,m=1 internal kink [4]. Until recently, this model has seemed a quite satisfactory basis for the interpretation of most stability results, even for high-β, shaped plasmas.

For the past few years, considerable attention has been focused on the stability of tokamaks with q on axis (q_0) near to and less than unity, and to the relation between MHD stability and the tokamak sawtooth [5–7]. The most recent studies have indicated that there are several problems with the interpretation of the sawtooth in terms of either ideal or non-ideal MHD stability [8]. Two recent studies [9,10] have also identified problems with the usual interpretation of numerical results in terms of circular cross-section, large aspect ratio analytic models such as the straight tokamak model. Specifically, when $q_0 < 1$, the n=1,m=1 *internal* kink in a straight cylinder ($n = 2\pi k R_0$ is a toroidal mode number and m is a poloidal mode number for a cylinder of length R_0) was shown to be stabilized by toroidal effects for sufficiently low β [4]. This has been verified in several numerical studies [11,12]. However, an

unstable "toroidal kink mode" still remains if the conducting wall is removed from the plasma surface [9]. Second, even though the cylindrical m=2 external kink, which occurs when the edge safety factor q_s is below 2.0, has an essentially unchanged stability limit at finite aspect ratio, several details of the mode structure are strongly modified by toroidal coupling of other poloidal components [10].

This work is intended to partly bridge the gap between the well-understood straight tokamak model and the present generation of finite aspect ratio, shaped tokamaks by analyzing, in detail, the role of toroidicity in the structure of current-driven modes in circular cross-section. Special attention is paid to the toroidal kink mode since it could play a role in the dynamics of the tokamak sawtooth cycle.

2. Equilibrium

The numerical studies discussed here were computed from solutions of the Grad-Shafranov equation,

$$\Delta^* \Psi = r j_\phi = - \left[r^2 p'(\Psi) + T(\Psi) T'(\Psi) \right] \quad , \tag{1}$$

using the EQLAUS code [13], in which either the flux surface integrated current density (the derivative of the current contained within a surface)

$$I'(\Psi) = \oint j_\phi \frac{d\ell}{|\nabla \Psi|} \quad , \tag{2a}$$

or the poloidally averaged current density

$$J(\Psi) = \oint j_\phi \frac{d\ell}{|\nabla \Psi|} \Big/ \oint \frac{d\ell}{|\nabla \Psi|} \quad , \tag{2b}$$

can be specified in place of the toroidal field function $T(\Psi) = r B_\phi$. Since consideration is restricted to current-driven modes, zero β is assumed. Furthermore, the equilibria are taken to have a circular cross-section since the main purpose of the work is to establish the link between the analytic straight tokamak model and real finite aspect ratio geometry.

Two types of current density profile are considered, corresponding to toroidal versions of the profiles analyzed by Shafranov [1] ("Shafranov-like" profiles) and by Wesson [2] ("Wesson-like" profiles). The Shafranov-like profiles are defined as

$$I'(\Psi) = \begin{cases} j_0 & \Psi < \Psi_c \quad , \\ \\ 0 & \Psi > \Psi_d \quad , \end{cases} \tag{3a}$$

with a cubic dependence on Ψ between Ψ_c and Ψ_d so that $I'(\Psi)$ is continuous. The cubic smoothing of the discontinuity from Ψ_c to Ψ_d was necessary for numerical reasons [13] but, in an effort to allow more variation in the profiles, the smoothing region could be extended considerably, in some cases up to 45% of the cross-section. The Wesson-like profiles are defined, with a slight modification to the code, in terms of an averaged current-density;

$$J(\Psi) = j_0 \left(1 - \left\langle \rho^2/\rho_b^2 \right\rangle\right)^\nu \quad . \tag{3b}$$

Here, ρ is the minor radius measured from the magnetic axis to the plasma boundary ρ_b and $\langle\ \rangle$ represents a flux surface average similar to that in Eq. (2b) but with $|\nabla\Psi|$ replaced by $B_p = |\nabla\Psi|/r$.

The profiles are shown in Fig. 1 as a function of the normalized flux variable [14] $s = [(\Psi - \Psi_0)/(\Psi_s - \Psi_0)]^{1/2}$, where Ψ_0 and Ψ_s are the flux at the magnetic axis and plasma edge, respectively. The parameters Ψ_c and Ψ_d in Eq. (3a) and ν in Eq. (3b) were varied to obtain several different equilibria. Varying these parameters effectively varies the global shear q_s/q_0. For each such equilibrium, the remaining parameter j_0 can be scaled to vary q_s without changing the flux surface geometry. In the process, the ratio q_s/q_0 and the shape of the q profile remain almost fixed, except at very low q_0. In the equilibrium code, j_0 is used to fit the prescribed toroidal current I_{tor}. Then j_0 is rescaled in the stability code ERATO [14]. In this way, both q_0 and q_s can be varied independently to span the parameter space shown in Fig. 2.

No real attempt was made in this study to accurately map out the stability boundaries in the (q_0, q_s) parameter space. Instead, the study concentrated on scanning equilibria in the vicinity of the constant q_s/q_0 lines labeled A, B, C, D, and E in Fig. 2. These particular q_s/q_0 values were strategically chosen to test for consistency of the stability picture with that of the straight tokamak. Several equilibria, with varying aspect ratios and current profile shapes, were taken about each line; the minor variations from each line result from the difficulty of obtaining a given ratio of q_s/q_0 with different aspect ratios or with different functional forms for the current profiles.

The stability of the numerically generated equilibria was determined by the ERATO stability code [14], which computes the growth rate γ of unstable modes, normalized to a toroidal Alfvén frequency $B_0/(R_0\sqrt{n_0\mu_0})$, where B_0 is the toroidal field and n_0 is the mass density at the magnetic axis $r = R_0$. Toroidal mode number $n = 1$ only was considered. In each case, the conducting wall was taken to be at infinity, except when wall stabilization was specifically tested for. The rectangular equilibrium mesh was taken at $N_r \times N_z = 200 \times 100$ and the equilibria were converged to machine accuracy. In the stability code, N_Ψ=80 flux surfaces and N_χ=40 poloidal angles were normally used. Considerable packing of the flux surfaces in important regions, particularly around the rational surfaces, was employed to increase the resolution of the code. Convergence studies were occasionally employed as a check on the resolution as well. In all the cases tested, however, the results obtained using careful packing of the flux surfaces with an 80×40 mesh were consistent with the fully converged result.

3. Discussion

3.1. Basic Stability Picture

The stability of the straight tokamak was reviewed in detail by Wesson [2] and by Freidberg [3], and can be summarized as follows. For $q_s < 2$, the plasma is unstable to an n=1,m=2 external kink. For $q_0 < 1$, the straight cylinder is unstable to an n=1,m=1 internal kink, but finite toroidicity stabilizes this mode, provided β is less than some critical β_c [4]. The third condition is a current-profile dependent condition of the form $q_s > \alpha(q_0)$ for stability against surface-localized or peeling modes with $m = [q_s] + 1$. Here, $\alpha(q_0)$ is a step-like function of q_0, and $[q]$ means the integer part of q. For step function "Shafranov" profiles,

$$j_\phi = \begin{cases} j_0 & \rho < \rho_c \quad , \\ \\ 0 & \rho \geq \rho_c \quad , \end{cases} \tag{4a}$$

where ρ is the minor plasma radius, the corresponding condition [1] is

$$q_s > [q_0] + 1 \quad , \tag{4b}$$

and for "Wesson" profiles [2],

$$j_\phi = j_0 \left(1 - \rho^2/\rho_b^2\right)^\nu \quad , \tag{5a}$$

the condition appears to be [2]

$$q_s > [2(q_0 - \delta)] + 2(q_0 - [q_0])\ S([q_0] - q_0 + \delta) + 1 \quad , \tag{5b}$$

where $\delta \sim 0.2$.

There are, however, three known modifications to this picture in real toroidal geometry. It was pointed out in Ref. 9 that a free boundary version of the n=1,m=1 internal kink can still be unstable at zero β when $q_0 < 1$. Furthermore, as was mentioned earlier, the detailed structure of the m=2 external kink can be quite different from the prediction of the straight tokamak model [10]. Thirdly, several recent studies have predicted [5] and identified [6] the existence of a so-called quasi-interchange mode which is unstable for $q_0 \gtrsim 1.0$ when the q profile has a large flat region near the center.

In this work we are primarily concerned with checking for broad consistency of the overall stability picture with that of the straight tokamak model; a complete determination of the stability boundary requires a more systematic scan of the parameter space than the one described here, with consistent sets of profiles coupled to detailed convergence studies. We will concentrate primarily on the effects of coupling, through toroidicity, of poloidal Fourier components of the unstable modes, the most important example being the toroidal kink mode, though mode coupling in the external and surface kinks also merits some attention. Although the quasi-interchange mode is a true toroidal mode, coupling of poloidal components is not the fundamental determinant of its stability; it depends, instead, on specific details of the q profile. Since it has already received a great deal of attention in the literature, it will not be addressed further in this study.

The results of the stability study using the numerical equilibria described in Section 2 are summarized in Fig. 2 in a so-called "Wesson diagram" [2] (drawn here on a linear scale in terms of q_0 and q_s), or "operational diagram" [15]. The data points used to generate this figure were taken specifically to test the stability boundaries $q_0 = q_c$ and $q_s = 2$ for both types of profile, and the boundary $q_s = \alpha(q_0)$ for the Wesson-like profile. The stability boundaries sketched in Fig. 2 do confirm the general stability picture described above. In particular, we find no change in the external kink boundary from $q_s = 2$, in agreement with Ref. 10, and the stability boundary for surface kinks has the expected qualitative form. Furthermore, we find the toroidal kink mode to be unstable for $q_0 < q_c \sim 1$ with a wall at infinity but stable when the wall is placed on the plasma boundary.

Several qualifications must, however, be made. First, the boundary $q_s = \alpha(q_0)$ for Shafranov-like profiles was not tested since, in order to compute numerical equilibria with the required low shear q profiles, the current profile needs to be flat over most of the plasma with an unresolvable gradient near the edge. The "Shafranov Profile" boundary shown in Fig. 2 is the straight tokamak result. Furthermore, even though it does have the same qualitative form, the equivalent boundary for the Wesson-like profiles does not exactly correspond to Eq. (5b). Shafranov [1] has shown that the growth rates of kink modes in a straight tokamak are of higher order than the finite aspect ratio corrections and, although a more detailed analysis [10] has shown that subtle cancellations can invalidate the argument in Ref. 1, the final conclusion still appears to hold. The stability boundary is therefore not expected to change markedly as a direct result of finite aspect ratio. It is, however, profile dependent as is clear from comparing Eqs. (5a) and (5b). In a finite aspect ratio torus, the profiles, Eqs. (3), can only approximately conform to those of Eqs. (4) or (5); the spatial current

distribution $j_\phi(r,z)$ is necessarily different to that of the straight tokamak. The shift in the stability boundary from the straight tokamak result, therefore, is probably largely due to this profile effect rather than to a direct toroidal effect. We do find, however, that the mode structure is considerably modified by the inclusion of toroidal coupling. This will be discussed in Subsection 3.3.

The boundaries shown in Fig. 2 are consistent with the data except, possibly, for one isolated point on the line labeled B, which appeared to be unstable, but is located in the region marked as stable. For that case, the mode was not well resolved (ERATO is generally numerically destabilizing) and the results of the convergence study were ambiguous. From recent studies in shaped cross-section tokamaks [15], it seems most likely that, if the point is truly unstable, it is also a profile rather than toroidal effect. This minor anomaly can be resolved by a more complete determination of the stability boundaries.

Finally, it must be mentioned that the stability boundary $q_0 = q_c$ for the toroidal kink mode is difficult to resolve, even with high resolution convergence studies. This problem will be addressed in the following subsection.

3.2. The Toroidal Kink Mode

When $q_0 < q_c$ in Fig. 2, the plasma is unstable to the toroidal kink mode. An example, corresponding to $q_0 = 0.50$, $q_s = 2.70$, and aspect ratio $R/a = 2.5$, is shown in Fig. 3a and the poloidal mode analysis of the contravariant perpendicular displacement $X = (q|\nabla\Psi|/T)\xi_\Psi$ is shown in Fig. 3b as a function of the flux coordinate s defined earlier in Section 2. The normalized growth rate for this case is $\gamma = 0.015$. Shown also in Fig. 3b is the surface-averaged integrand $W(\Psi)$ for the ideal MHD, perturbed potential energy in the plasma;

$$\delta W_{\rm p} = \int W(\Psi)\, d\Psi$$

$$= \frac{1}{2}\int \frac{|\delta B|^2}{4\pi} - \underline{\xi}\cdot\underline{j}\times\delta\underline{B} + \underline{\xi}\cdot\underline{j}\times\underline{B}\nabla\cdot\underline{\xi} + \gamma p\left|\nabla\cdot\underline{\xi}\right|^2 d^3\underline{r} \quad . \qquad (6)$$

The equilibrium corresponding to Figs. 3a and 3b is indicated in Fig. 2 as the point marked by a circled x and labeled (a).

The mode structure is dominated by the n=1,m=1 component within the q=1 surface. Note that $X \sim s\xi_\Psi$ inside $q = 1$ so that ξ_Ψ corresponds to the step function displacement characteristic of an internal kink. This is coupled to an m=2 component maximized between the q=1 and q=2 surfaces. In contrast to the model of Ref. 4, the m=2 component is not constrained to vanish but remains finite out to the plasma boundary. Moreover, the m=3 component is not only finite, but is maximized with a considerable amplitude at the plasma boundary. This component is reminiscent of the straight tokamak surface kink mode. It should also be noted that there is a finite m=4 component, as well as other smaller, higher order components that are finite near the edge, but these are omitted in Fig. 3b. Coupling of the surface kink component with the internal kink-like m=1,2 components appears to be the crucial element in the destabilization of the toroidal kink mode. In Ref. 4, the m=3 component of the internal kink mode is forced (with the other components) to vanish at the boundary and is then of higher order than the m=1 and m=2 components.

When $q_s < 2$, the m=2 component is maximized and dominant at the boundary instead of the m=3 component, but otherwise the structure is basically similar. An example displaying the essential features [the point marked (b) in Fig. 2] is shown in Figs. 4a and 4b. For this case, $q_0 = 0.29$, $q_s = 1.18$, $R/a = 5.0$, and $\gamma = 0.044$. In this

example, the m=3 component is, in fact, negligible and is not shown. For both $q_s < 2$ and $q_s > 2$, when the wall is moved on to the plasma surface, thereby constraining the surface perturbation amplitude, the toroidal kink mode is stabilized as predicted in Ref. 4.

The mode plots in Figs. 3a and 4a are typical of the toroidal kink mode: an internal kink-like structure inside $q = 1$, with a large poloidally directed displacement near the q=1 surface, smaller maxima at successive integral q surfaces, and little visible displacement elsewhere. The displacement near $q = 1$ dominates the kinetic energy. The form of $W(\Psi)$ in is also typical with a destabilizing [negative $W(\Psi)$] core surrounded by a stabilizing shell out to the q=1 surface, which is characteristic of an internal kink, plus small stabilizing contributions that are maximized between successive integral q surfaces. As the value of q_s is increased, more layers are added which shield the internal kink region from the edge. The extra positive contributions to δW, together with the added kinetic energy contribution at new integer q surfaces, should result in a corresponding drop in the growth rate as q_s passes through integral values. This is generally, though not always, found to be the case in the numerical studies.

Before turning to the scaling of the toroidal kink mode, there are several objections that might be raised to its interpretation as being an internal kink destabilized by toroidal coupling and the free boundary. First, even though the outer boundary is a circular cross-section, the elongation κ of the central flux surfaces is generally slightly greater than 1.0, the maximum being 1.023. At the q=1 surface, the elongation is between that at the center and that at the edge and the triangularity is negligible. The toroidal kink mode is not, however, the internal kink that is predicted to be unstable in elongated cross-sections [16,17]. The criterion for *instability* of the internal

kink [16,17] is equivalent to a condition of the form $q_c \leq q_0 \leq 1$, in contrast to the corresponding criterion for instability of the toroidal kink, $q_0 \leq q_c \lesssim 1$. Furthermore, when the wall is placed on the plasma surface, the growth rates drop to unresolvable values, so, although some remnant of the internal kink might still be unstable with a small growth rate, it is clearly not directly related to the toroidal kink mode that is observed when the wall is at infinity.

Two potentially more serious objections are that the example shown in Figs. 3a and 3b for $q_s > 2$ has a slightly hollow q profile and corresponds to an equilibrium with a special Shafranov-like profile. The example in Figs. 4a and 4b, in which q is monotonic and the current profile is given by Eq. (3b), could be argued to be a special case since equilibria with $q_s < 2$ are already known to be unstable to a free boundary kink mode [1]. Moreover, for equilibria in which the Wesson-like profiles were used and the q profiles were monotonic when $q_0 < 1$ and $q_s > 2$, the growth rates were always much smaller than, and the modes seldom as broadly resolved as, the example in Fig. 3a. However, the hollow q profile for the example in Figs. 3a and 3b is unlikely to contribute significantly since it would more likely couple $m = -1$ with $m = +1$. The m=−1 component is entirely negligible in most cases, including that shown in Fig. 3b, although coupling to $m = -1$ was observed in some cases with quite hollow q profiles. The special profile is also unlikely to be significant, since the Shafranov-like profile used for the equilibrium shown is highly modified, with rounding implemented from the 20% flux surface to the 65% flux surface.

Nevertheless, the objections should still be fully addressed. Figures 5a, 5b, and 5c show an example of a toroidal kink mode obtained with a Wesson-like profile ($\nu = 3.2$, $q_0 = 0.85$, $q_s = 3.78$, and aspect ratio $R/a = 5.0$). This equilibrium has a monotonic q profile and corresponds to the point labeled (c) in Fig. 2. The normalized

growth rate for this case is $\gamma = 0.0036$. The mode plot in Fig. 5a shows an almost singular structure around $q = 1$, but high resolution around the q=1 surface reveals that the structure is actually finite. The poloidal Fourier analysis of the perpendicular displacement shown in Fig. 5b is again typical of a toroidal kink mode. The m=1 component is dominant with its support almost entirely within $q = 1$. This is coupled to m=2 and 3 components, with support mostly within each respective q=(m+1)th surface, and to an m=4 component which increases in amplitude out to the edge of the plasma. The m=1, 2, and 3 components also remain finite, though very small, at the plasma edge.

Shown in Fig. 5c is the flux surface averaged kinetic energy

$$K(\Psi) = \frac{1}{2} \int n_{\mathrm{p}} \left|\underline{\xi}\right|^2 \frac{d\ell}{B_{\mathrm{p}}} \quad . \tag{7}$$

Here, n_{p} is the plasma density, B_{p} is the poloidal magnetic field, and the integral is around the flux surface Ψ. The total kinetic energy is dominated by the contribution from the immediate vicinity of $q = 1$, though there are small, almost negligible, but nonetheless important, contributions from other integral surfaces and from the edge. The poloidal component of the displacement is the dominant contribution to $K(\Psi)$, and the contravariant part perpendicular to both $\underline{B}$ and $\nabla\Psi$, $Z = (s|\nabla\Psi|/r)(\xi_\chi - B_{\mathrm{p}}/B_\phi \xi_\phi) + (\nabla\Psi \cdot \nabla\chi)/|\nabla\Psi|^2 X$, is also shown in Fig. 5c. The m=1 Fourier component is, by far, the largest; the higher m components are considerably magnified in Fig. 5c. The data points are also shown to indicate that, although the structures around the integral surfaces are quite narrow, they are of finite width and quite well resolved.

For a single equilibrium, q_0 and q_s can be scaled by varying the constant j_0 in Eqs. (3), thereby generating several equilibria along a line such as those shown in Fig. 2. The scaling of the square of the normalized growth rate γ^2 (the eigenvalue from ERATO) versus q_s for such a sequence, along line A in Fig. 2, is given in Fig. 6. The three curves were generated for equilibria with the same Shafranov-like current profile ($\Psi_c = 0.20$, $\Psi_d = 0.65$) and different values of the aspect ratio: $R/a = 10.0$, 5.0, and 2.5. The case $R/a = 2.5$ with $q_s = 2.70$ corresponds to the equilibrium of Fig. 3a. Each of the points shown has $q_0 < 1$; the numbers associated with the points are q_0 and, if the q profile is hollow, $q_{\min}$.

For $q_s > 1$, the unstable modes are global n=1,m=1 kinks and the growth rates are essentially independent of aspect ratio. When $q_s > 1$, however, the unstable modes are toroidal kinks. As the growth rate decreases, either by raising q_s or increasing the aspect ratio, the width of the structure around the q=1 surface (in Fig. 3a, for example) becomes increasingly more narrow and, in the marginal stability limit, the mode becomes a singular Mercier-like mode.

Despite the increasing unreliability of the growth rates below $\gamma^2 \sim 10^{-5}$, the overall scaling with aspect ratio can be extracted from Fig. 6; for $1 < q_s < 2$, the three curves are displaced by a factor $2^4 = 16$ and for $2 < q_s < 3$, allowing for the decreasing accuracy when $\gamma^2 < 10^{-5}$, the factor is close to $2^8 = 256$. Taking the global kink into account, the scaling is therefore well described by

$$\gamma^2 \propto h\,(q_0, q_s)\,(a/R)^{4[q_s]} \quad , \tag{8}$$

where $h(q_0, q_s)$ contains the dependence on the current profile. The straight tokamak limit with $a/R \to 0$ has $\gamma^2 \to 0$ as one would expect if the mode is truly driven by

toroidal coupling. Note that the toroidal kink mode is more unstable at low aspect ratio in the sense that the growth rates are larger, although there is no evidence that the marginal stability criterion depends on the aspect ratio.

Since the growth rates γ scale with $(a/R)^{2[q_s]}$, they can be quite small for moderate a/R and q_s values. The function $h(q_0, q_s)$ appears to be quite strongly dependent on the form of the current profile, making the stability boundary even more difficult to determine. In the cases analyzed in this study, the plasma was definitely unstable whenever $q_0 < 0.65$ and whenever $q_s < 2$. On the other hand, no conclusively unstable case has been found in circular cross-section for $0.90 < q_0 < 1$ when $q_s > 2$. In the region $0.65 < q_0 < 0.90$, several cases were definitely unstable and others were indeterminate, having growth rates beyond the limit of resolution. Convergence studies are not normally effective in determining the stability of toroidal kink modes, since they seldom converge quadratically and the extrapolated eigenvalue is sensitive to numerical noise in the convergence plot. The stability limit q_c is therefore not well defined, probably lying somewhere in the range between 0.85 and 1.0. It could naively be expected that the mode remains unstable as long as the q=1 surface remains within the plasma and couples to the edge m=($[q_s]$+1) component. The limit would then be $q_0 = 1$. In any case, however, the limit in circular cross-section is a soft limit in the sense that, if the limit is $q_0 \simeq 1$, the growth rates remain very small as q_0 decreases until $q_0 \sim 0.85$ and, if the limit is $q_0 = q_c < 1$, it is quite profile dependent.

3.3. Other Modes

In contrast to the toroidal kink mode, the stability condition $q_s < 2$ for the external kink is a hard limit. A typical example, corresponding to the point labeled (d) in Fig. 2 with aspect ratio $R/a = 2.5$, $q_0 = 1.06$, $q_s = 1.731$, and $\gamma = 0.21$ is

given in Figs. 7a and 7b. This example was computed using the Wesson-like profile with $\nu = 0.5$. Figure 7a shows the vector plot of the mode displacement, with the dominant m=2 component maximized at the plasma surface. The poloidal m=1, m=2, and m=3 components of the perpendicular displacement are shown in Fig. 7b. The detailed structure of a similar example was analyzed in Ref. 10, where it was shown that, while the q_s=2 stability limit is not changed by coupling of the m=2 component with the other poloidal components, $\delta W_{22} \equiv \delta W(\xi^{m=2}, \xi^{m=2})$ can be positive for aspect ratios less than 10 and δW_{33} can even be larger than δW_{22}. The destabilizing negative contributions are provided by the off-diagonal terms. Even though the m=2 component of $\underline{\xi}$ is dominant, the other poloidal components cannot therefore be neglected except at very large aspect ratio.

For the same Wesson-like profile, Eq. (3b), several well resolved unstable surface kink modes were found by scaling j_0 in a sequence roughly corresponding to the line E in Fig. 2. An example is shown in Figs. 8a and 8b, corresponding to the point labeled (e) in Fig. 2. This case has $q_0 = 2.75$, $q_s = 4.85$, and a normalized growth rate of $\gamma = 0.028$. The m=5 component is dominant and highly localized near the edge, as expected from the straight tokamak prediction, but here the m=4 component is still considerable. The other components are also finite and, especially the m=3 component, not entirely negligible. The m=3 component has two independent lobes, an internal kink-like part inside $q = 3$ and a surface kink-like component outside $q = 3$. These two parts are apparently coupled via toroidal coupling through the other Fourier components.

Shown also in Fig. 8b is the integrand $W(\Psi)$ of δW_p [Eq. (6)]. The destabilizing contribution comes from most of the plasma volume except from the very edge. The basic structure of the mode is similar to that of the external kink in Figs. 7a and 7b,

though it is much more localized near the edge; it is basically the higher m version of the same mode. This is essentially the prediction of the straight tokamak model. Despite this, toroidal coupling clearly has a considerable effect on the structure.

By taking scans with varying j_0 [Eq. (3)], and constant q_s/q_0 as discussed in Section 2, transitions from one type of mode to another can be seen. Figure 9 shows the growth rate scaling γ^2 versus q_s for three classes of equilibrium configuration with $q_s/q_0 \gg 2$ (line labeled A in Fig. 2) $q_s/q_0 \gtrsim 2$ (B in Fig. 2), and $q_s/q_0 < 2$ (D in Fig. 2). Each of these has aspect ratio $R/a = 2.5$ and Shafranov-like profiles with $\Psi_c = 0.20$, $\Psi_d = 0.65$ (line A), $\Psi_c = 0.45$, $\Psi_d = 0.65$ (line B), and $\Psi_c = 0.65$, $\Psi_d = 0.95$ (line D) were used. When $q_s < 1$, the unstable modes are again n=1,m=1 global kinks, essentially unmodified from the straight tokamak prediction. The normalized growth rates are comparable for the three cases; the global kink mode is largely independent of both the current profile and the aspect ratio.

When $q_s > 1$, the mode undergoes a rapid transition to a toroidal kink mode. The n=1,m=1 kink structure remains inside the q=1 surface, but the amplitude decays rapidly outside. The m=2 component becomes important and the poloidal component of $\underline{\xi}$ around $q = 1$ becomes dominant. The growth rate becomes strongly dependent on both the current profile and the aspect ratio.

As q_s is increased further by scaling j_0, one of two possibilities occurs. When $q_s/q_0 > 2$, the toroidal kink remains the dominant structure up to and beyond $q_s = 2$. On the other hand, when $q_s/q_0 \lesssim 2$, the mode undergoes a transition to an external kink as the m=2 Fourier component becomes dominant. The growth rate begins to increase with q_s and peaks when $q_0 = 1$. Then, as q_s approaches 2, the m=2 edge structure becomes increasingly more localized and the growth rate drops rapidly,

vanishing when $q_s = 2$. The transition point between the toroidal kink (TK) and external kink (EK) is indicated for this case in Fig. 9.

A similar sequence holds for the Wesson-like profiles. Figures 10a and 10b show the mode structure for a transition case between the toroidal and external kink. This example was computed with the Wesson-like profile for $\nu = 1.0$ at $R/a = 2.5$, and corresponds to $q_0 = 0.716$, $q_s = 1.526$. This is the point labeled (f) in Fig. 2. The normalized growth rate is $\gamma = 0.069$. The transition to the external kink is rapid; when q_s is increased to just 1.879 ($q_0 = 0.844$), the unstable mode is an unmodified external kink like that shown in Figs. 7a and 7b.

3.4. Effect of Elongation

Although this study is primarily concerned with circular cross-section, it is useful to consider briefly the effect of elongation on the stability of the toroidal kink mode. Figures 11a and 11b show the structure of the toroidal kink mode in an elliptical cross-section with elongation $\kappa = 1.5$. This case corresponds to a Shafranov-like profile with $R/a = 2.5$, $q_0 = 0.656$, and $q_s = 4.64$ and is marked on Fig. 2 as the point labeled (g). The structure is the same as that in circular cross-section. The instability is, however, greatly enhanced with a normalized growth rate of $\gamma = 0.011$. In circular cross-section, few cases with $q_s > 3$ were unambiguously unstable and it was impossible to resolve any case with $q_s > 4$.

Several recent studies [15,18,19] have partly extended the study described here to more strongly shaped cross-sections. In Ref. 15, the stability limit for the toroidal kink mode was found to be a hard limit at $q_0 = 1$ for both racetrack and dee-shaped cross-sections with elongation $\kappa = 2.5$. The growth rates were also several orders of magnitude greater than those found here for circular cross-section. For a band near

$q_0 = 1$, Laval [16] has shown that, when $\kappa > 1$, the plasma can be unstable to a true internal kink mode. Thus, the stability limit is expected to be $q_0 = q_c = 1$ as was found in Ref. 15. In the studies in Refs. 15, 18, and 19, only the free boundary versions of the internal modes were computed and these were not distinguished from the toroidal kink. Finite triangularity and lower elongation than the case considered in Ref. 15, while known to stabilize the internal kink [16,17], also appear to soften the stability limit for the toroidal kink [18,19]. A finite region $q_c < q_0 < 1$ for $q_c \sim 0.7$ can probably be stabilized, although, as in the study discussed here, the convergence properties and low growth rates of the mode make any definite estimate for q_c difficult to justify.

At finite β, with a value dependent on the cross-section, the internal kink becomes unstable and, in the standard Kadomtsev model [20], this mode (or at least its resistive counterpart) is invoked as the cause of the sawtooth crash. However, comparison of the crash timescale with the growth rates of the internal kink still leave a sizeable factor to be explained [5]. The toroidal kink mode also exists at finite β in the sense that the free boundary mode is more unstable than the corresponding internal kink and exhibits the toroidal coupling that is characteristic of the toroidal kink mode at zero β. This is also true if a finite wall and vacuum region are present. Taking account of the real wall position could therefore resolve part of the discrepancy in the timescales predicted by the Kadomtsev model. In any case, it can be expected that the toroidal kink mode will play a more important role in the stability and, possibly, in the operation [19] of finite β, non-circular tokamaks.

4. Conclusions

The main conclusions from this work can be summarized as follows. In circular cross-section toroidal geometry, the stable operational space at $\beta = 0$ is limited to $q_s > 2$, to $q_0 > q_c$ where $q_c \lesssim 1$, and to $q_s/q_0 < \alpha(q_0)$. When $q_s < 2$, the unstable mode is the n=1,m=2 external kink, modified from the prediction of the straight tokamak model by coupling of other poloidal components through toroidicity. When $q_0 < q_c$, the plasma is unstable to the free boundary toroidal kink mode. This mode is a truly toroidal mode; it consists of an n=1,m=1 internal kink coupled through toroidicity to m=2,3...$[q_s]$+1 poloidal components, where the $m=[q_s]+1$ surface kink-like component remains finite at the edge of the plasma. The limit q_c is a soft limit in circular cross-section, but increased elongation can greatly enhance the instability and destabilize a true internal kink, creating a hard limit at $q_0 = q_c = 1$. Further work is in progress to determine the role, if any, that the toroidal kink mode plays in the tokamak sawtooth and in the recent observations, that for some tokamaks, q_0 is significantly below unity [7].

When $q_s/q_0 < \alpha(q_0)$, the unstable modes are $m=[q_s]+1$ surface kinks and are predicted by the straight tokamak model. At finite aspect ratio, they are considerably modified by coupling of other poloidal components. Although the qualitative form appears to be unchanged, the boundary $\alpha(q_0)$ is different from the prediction of the straight tokamak model. Since $\alpha(q_0)$ is known to depend on the current profile, it has not been determined whether the change is a direct result of toroidal coupling

or is induced via toroidal effects on the spatial current distribution $j_\phi(r,z)$. The indications are, however, that the current profile effects are most important. The detailed stability boundary needs to be determined by a more complete systematic stability survey.

Acknowledgments

The authors wish to acknowledge the support and encouragement of several colleagues, in particular Dr. A. Pochelon. Also, discussions with Dr. J.A. Wesson were greatly appreciated. This work was supported by the Swiss National Science Foundation and, in part, by the U.S. Department of Energy under Contract No. DE-AT03-84ER53158.

References

[1] SHAFRANOV, V.D., Sov. Phys.-Tech. Phys. **15** (1970) 175.

[2] WESSON, J.A., Nucl. Fusion **18** (1978) 87.

[3] FREIDBERG, J.P., Rev. Mod. Phys. **54** (1982) 801.

[4] BUSSAC, M.N., EDERY, D., PELLAT, R., SOULÉ, J.L., Phys. Rev. Lett. **35** (1975) 1638.

[5] WESSON, J.A., Plasma Phys. and Contr. Fusion **28** (1986) 243.

[6] RAMOS, J., Phys. Rev. Lett. **60** (1988) 523; WAELBROECK, F.L., HAZELTINE, R.D., Phys. Fluids **31** (1988) 1217; NAVE, M.F.F., WESSON, J.A., Nucl. Fusion **28** (1988) 297; AYDEMIR, A.Y., Phys. Rev. Lett. **59** (1987); HASTIE, R.J., HENDER, T.C., CARRERAS, B.A., CHARLTON, L.A., HOLMES, J.A., Phys. Fluids **30** (1987) 1756; KIRBY, P., Nucl. Fusion **28** (1988) 231.

[7] SOLTWISCH, H., STODIEK, W., MANICKAM, J., SCHLÜTER, J., in Plasma Physics and Controlled Nuclear Fusion Research (Proc. 11th Int. Conf. Kyoto, 1986) Vol. 1, IAEA, Vienna (1987) 263.

[8] WESSON, J.A., in Proc. 1988 Sherwood Theory Meeting (Annual Controlled Fusion Theory Conference, Gatlinburg, 1988) Oak Ridge National Laboratory, Oak Ridge, Tennessee; HASTIE, R.J., HENDER, T.C., Nucl. Fusion **28** (1988) 585; AYDEMIR, A.Y., WILEY, T.C., ROSS, D.W., Phys. Fluids B **1** (1989) 774.

[9] TURNBULL, A.D., TROYON, F., in Proc. 12th Euro. Conf. on Controlled Fusion and Plasma Physics (Budapest, 1985), Supplement to the Proceedings, Part 1, 48.

[10] SCHULTZ, G., TROYON, F., TSUNEMATSU, T., BONDESON, A., ROY, A., in Theory of Fusion Plasmas (Proc. Workshop held at Villa-Cipressi-Varenna, Italy, August 1987) (BONDESON, A. *et al.*, Eds.) Editrice Compositori, Bologna (1988) 77.

[11] KERNER, W., GRUBER, R., TROYON, F., Phys. Rev. Lett. **44** (1980) 536.

[12] MANICKAM, J., Nucl. Fusion **24** (1984) 595.

[13] TURNBULL, A.D., SECRÉTAN, M.A., TROYON, F., SEMENZATO, S., GRUBER, R., J. Comp. Phys. **66** (1986) 391.

[14] GRUBER, R., TROYON, F., BERGER, D., BERNARD, L.C., ROUSSET, S., *et al.*, Comput. Phys. Commun. **21** (1981) 323.

[15] ROY, A., TURNBULL, A.D., SAUTER, O., NICLI, S., TROYON, F., in Proc. 13th Euro. Conf. on Controlled Fusion and Plasma Heating Schliersee (1986) 77; TURNBULL, A.D., ROY, A., SAUTER, O., TROYON, F., Nucl. Fusion **28** (1988) 1379.

[16] LAVAL, G., Phys. Rev. Lett. **34** (1975) 1316.

[17] EDERY, D., LAVAL, G., PELLAT, R., SOULÉ, J.L., Phys. Fluids **19** (1976) 260.

[18] TURNBULL, A.D., YASSEEN, F., ROY, A., SAUTER, O., COOPER, W.A., *et al.*, General Atomics Rep. GA-A19193 (1988), to be published in Nucl. Fusion.

[19] TURNBULL, A.D., CHU, M.S., GREENE, J.M., HELTON, F.J., to be published.

[20] KADOMTSEV, B.B., Fiz. Plasmy **1** (1975) 710 [Sov. J. Plasma Physics **1** (1975) 389].

Figure Captions

FIG. 1. Typical Shafranov-like current density profile $I'(\Psi)$ (solid line) corresponding to $\Psi_c = 0.20$ and $\Psi_d = 0.65$ and Wesson-like profile $J(\Psi)$ (dashed line) corresponding to $\nu = 3.2$ as functions of the normalized flux variable $s = [(\Psi - \Psi_0)/(\Psi_s - \Psi_0)]^{1/2}$. Shown also are the safety factor profiles q with j_0 normalized so that $q_0 \simeq 1$.

FIG. 2. Circular cross-section operational diagram in (q_0, q_s) parameter space. The equilibria used in this study were generated to lie approximately along the lines labeled A to E. Shown also are the straight tokamak stability boundaries (short dashed lines) for "Wesson" and "Shafranov" profiles and the approximate stability boundary obtained from this study (solid line).

FIG. 3a. Displacement vector plot for the toroidal kink mode with $2 \leq q_s \leq 3$ ($q_0 = 0.50$, $q_s = 2.70$), obtained with the Shafranov-like profile ($\Psi_c = 0.20$, $\Psi_d = 0.65$) at $R/a = 2.5$.

FIG. 3b. Potential energy $W(\Psi)$ and poloidal Fourier components of the perpendicular displacement X (m = 1,2,3) corresponding to the toroidal kink mode shown in Fig. 3a. The radial coordinate is the normalized flux variable $s = [(\Psi - \Psi_0)/(\Psi_s - \Psi_0)]^{1/2}$. Also shown for reference is the q profile with the scale on the right.

FIG. 4a. Displacement vector plot for the toroidal kink mode with $1 \leq q_s \leq 2$ ($q_0 = 0.29$, $q_s = 1.18$), obtained with the Wesson-like profile ($\nu = 3.2$) at $R/a = 5.0$.

FIG. 4b. Potential energy $W(\Psi)$ and poloidal Fourier components of X (m = 1,2,3) versus s for the toroidal kink mode in Fig. 4a. The q profile is also shown for reference.

FIG. 5a. Displacement vector plot for the toroidal kink mode with $3 \leq q_s \leq 4$ ($q_0 = 0.85$, $q_s = 3.78$), obtained with the Wesson-like profile ($\nu = 3.2$) at $R/a = 5.0$.

FIG. 5b. Potential energy $W(\Psi)$ and poloidal Fourier components of X (m = 1,2,3,4) versus s for the toroidal kink mode in Fig. 5a. The m = 2,3,4 components have been magnified here by a factor of 10 compared to $m = 1$. The q profile is also shown for reference.

FIG. 5c. Kinetic energy $K(\Psi)$ and poloidal Fourier components of the poloidal displacement Z (m = 1,2,3,4) versus s for the toroidal kink mode in Fig. 5a. The m=2,3,4 components have been magnified here by factors of 20 (m = 2) and 100 (m = 3,4). The zero point for $K(\Psi)$ is the lower horizontal axis.

FIG. 6. Growth rate scaling of the toroidal kink mode versus q_s for different aspect ratios R/a = 2.5 (solid line), 5.0 (long dashes), and 10.0 (short dashes) obtained using the Shafranov-like profile ($\Psi_c = 0.2$, $\Psi_d = 0.65$).

FIG. 7a. Displacement vector plot for the external kink mode with $q_0 > 1$ and $q_s < 2$ ($q_0 = 1.06$, $q_s = 1.73$), obtained with the Wesson-like profile ($\nu = 0.5$) at $R/a = 2.5$.

FIG. 7b. Potential energy $W(\Psi)$ and poloidal Fourier components of X (m = 1,2,3) versus s for the external kink mode shown in Fig. 7a. The q profile is also shown for reference.

FIG. 8a. Displacement vector plot for the surface kink mode with $q_0 = 2.75$ and $q_s = 4.85$, obtained with the Wesson-like profile ($\nu = 0.5$) at $R/a = 2.5$.

FIG. 8b. Potential energy $W(\Psi)$ and poloidal Fourier components of X ($m = 1$ to 6) versus s for the surface kink mode shown in Fig. 8a. The q profile is also shown for reference.

FIG. 9. Growth rate scaling versus q_s for three different Shafranov-like profiles at $R/a = 2.5$ generated by scaling q_s along the lines A (solid line), B (long dashes), and D (short dashes) of Fig. 2.

FIG. 10a. Displacement vector plot for the transition toroidal kink/external kink mode with $q_0 = 0.72$ and $q_s = 1.53$, obtained with the Wesson-like profile ($\nu = 1.0$) at $R/a = 2.5$.

FIG. 10b. Potential energy $W(\Psi)$ and poloidal Fourier components of X (m = 1,2,3) versus s for the transition toroidal kink/external kink shown in Fig. 10a. The q profile is also shown for reference.

FIG. 11a. Displacement vector plot for the toroidal kink mode in elongated cross-section ($\kappa = 1.5$) with $q_0 = 0.66$ and $q_s = 4.64$, obtained with the Shafranov-like profile ($\Psi_c = 0.2$, $\Psi_d = 0.65$) at $R/a = 2.5$.

FIG. 11b. Potential energy $W(\Psi)$ and poloidal Fourier components of X ($m = 1$ to 5) versus s for the toroidal kink mode shown in Fig. 11a. The q profile is also shown for reference.

Turnbull
CRPP
Fig. 1

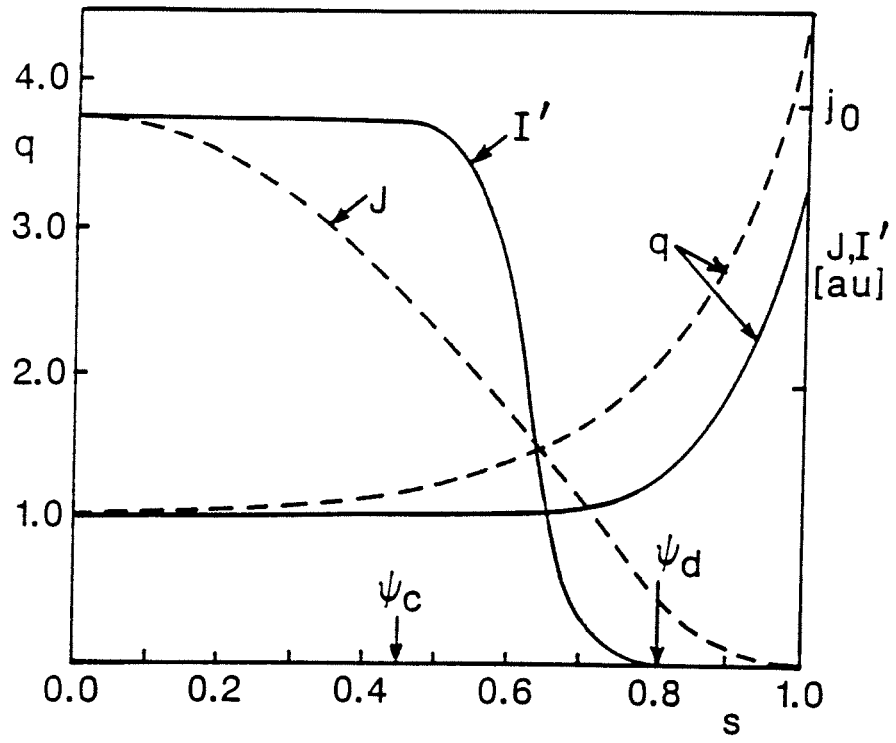

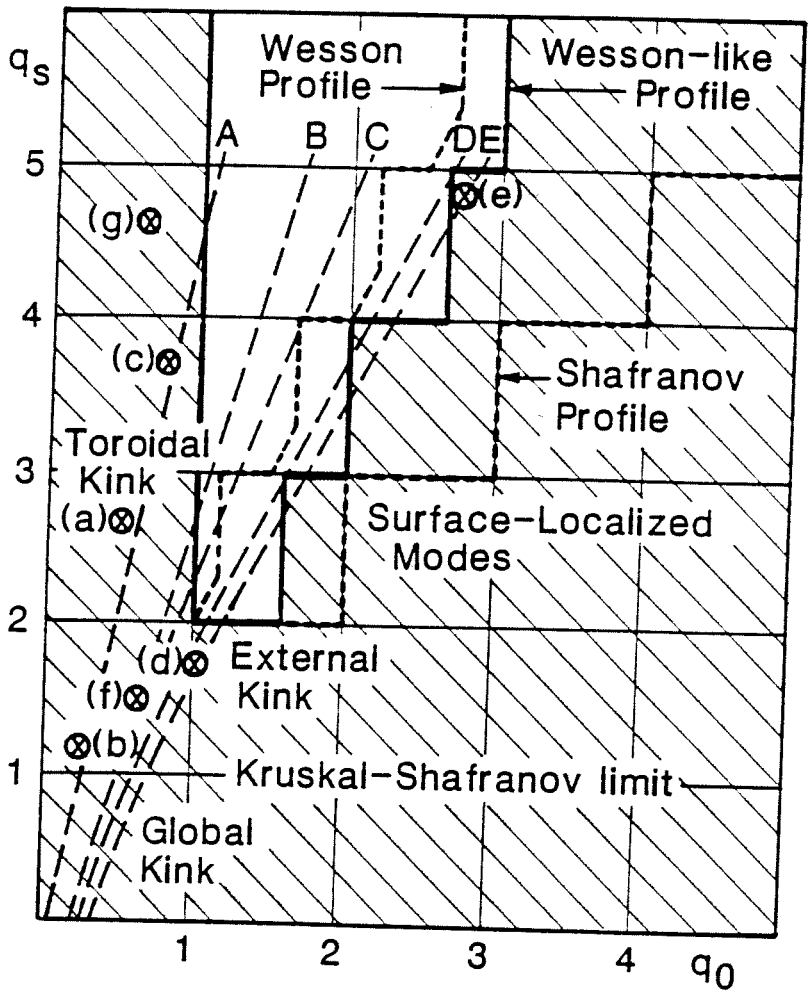
q_s
Wesson
Profile
Wesson-like
Profile
A
B
C
DE
5
(g)
(e)
4
(c)
Shafranov
Profile
Toroidal
Kink
3
(a)
Surface-Localized
Modes
2
(d)
External
Kink
(f)
(b)
1
Kruskal-Shafranov limit
Global
Kink
1
2
3
4
q_0

Turnbull
CRPP
Fig. 3a

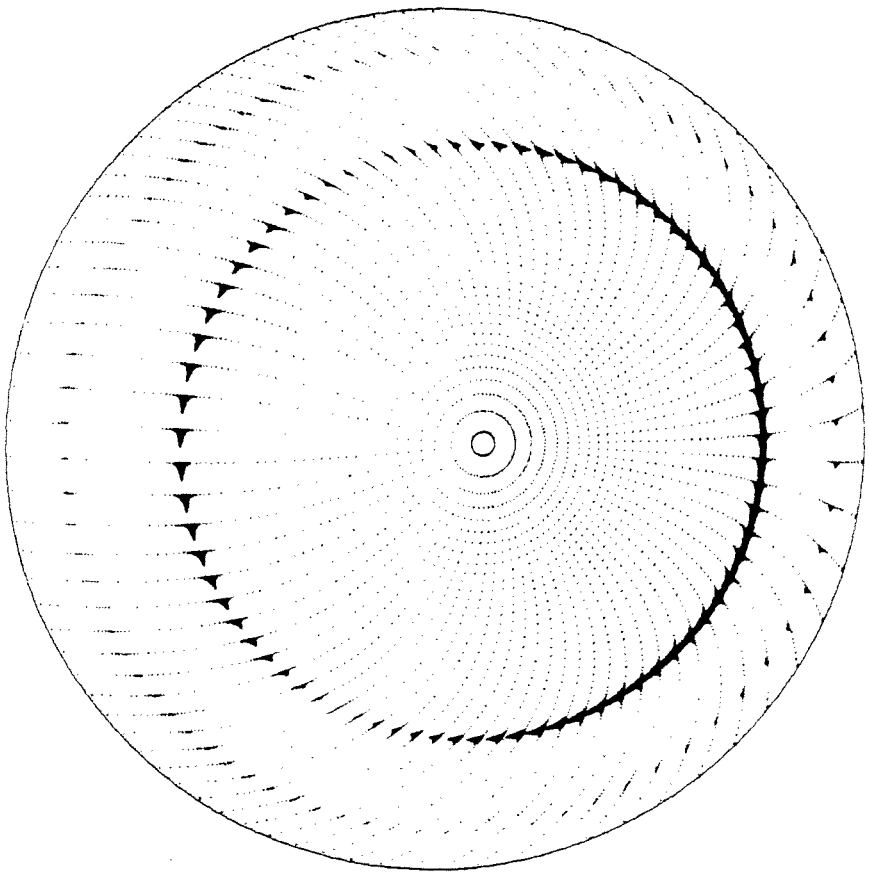

Turnbull
CRPP
Fig. 3b

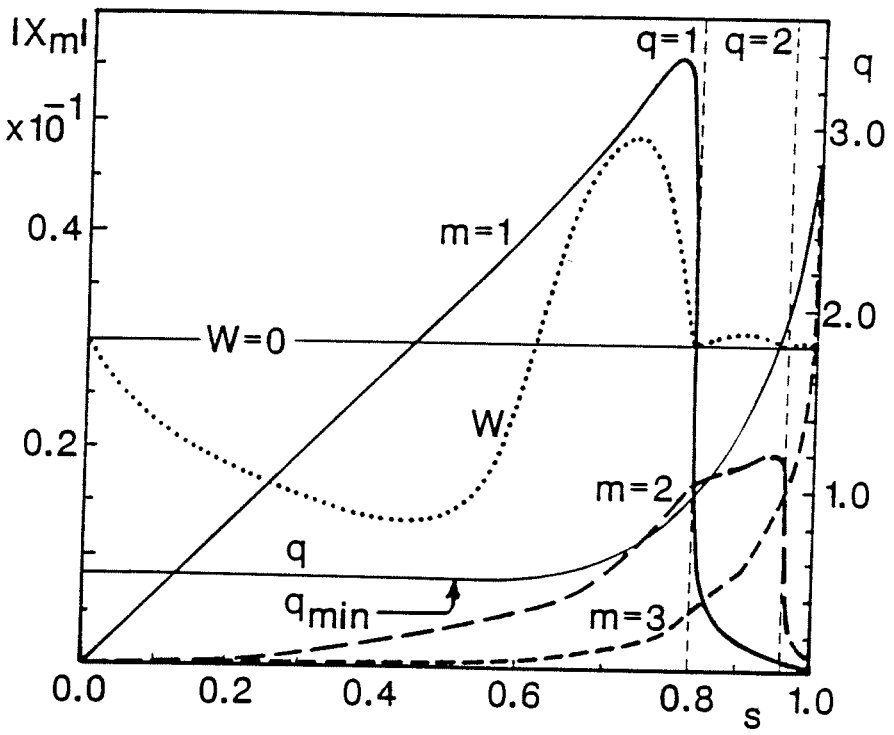

Turnbull
CRPP
Fig. 4a

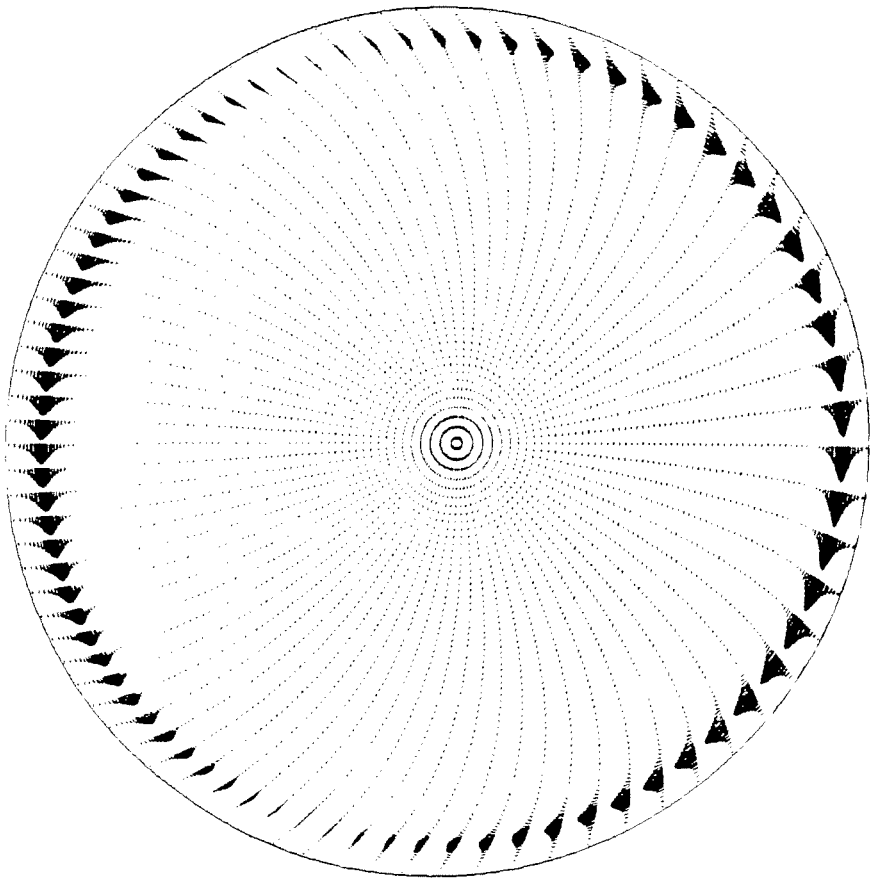

Turnbull
CRPP
Fig. 4b

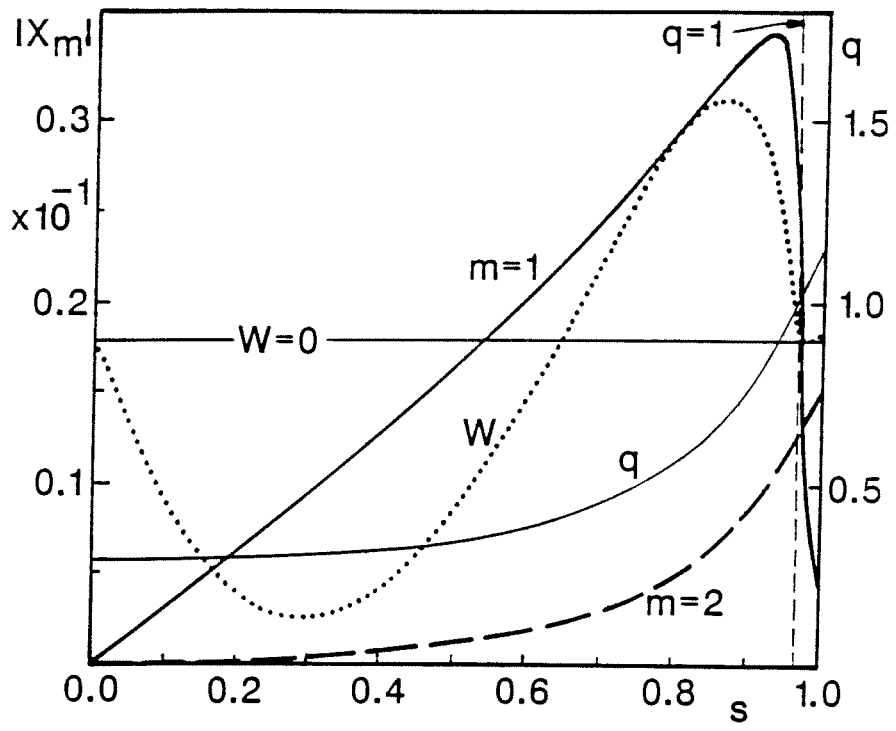

Turnbull
CRPP
Fig. 5a

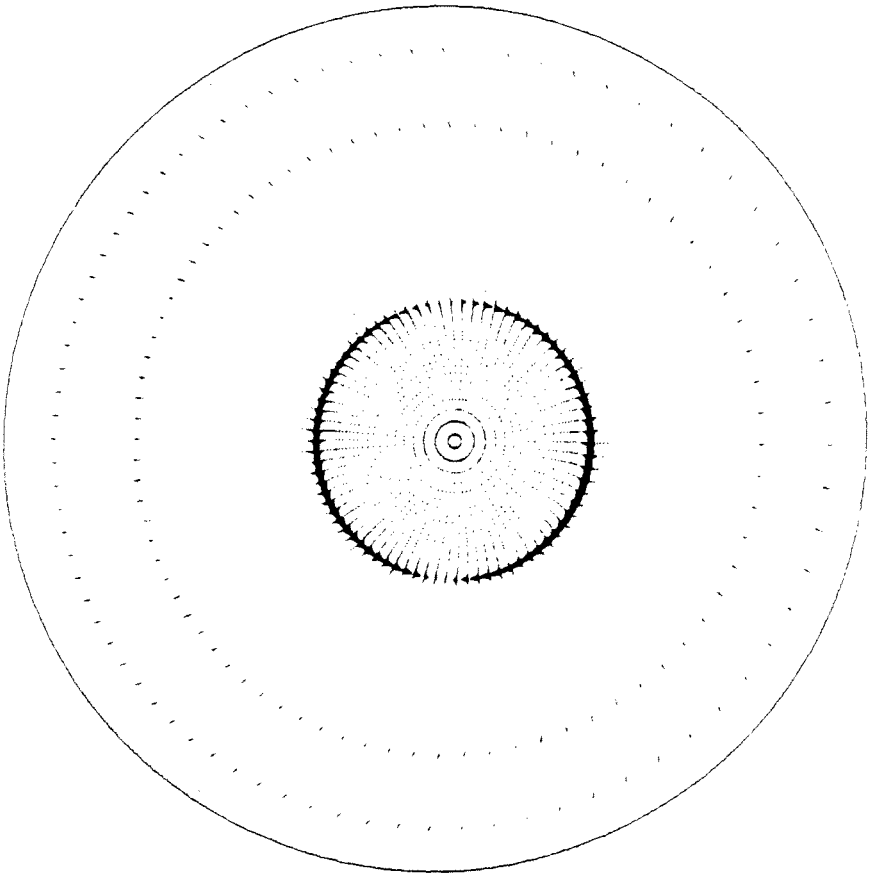

Turnbull
CRPP
Fig. 5b

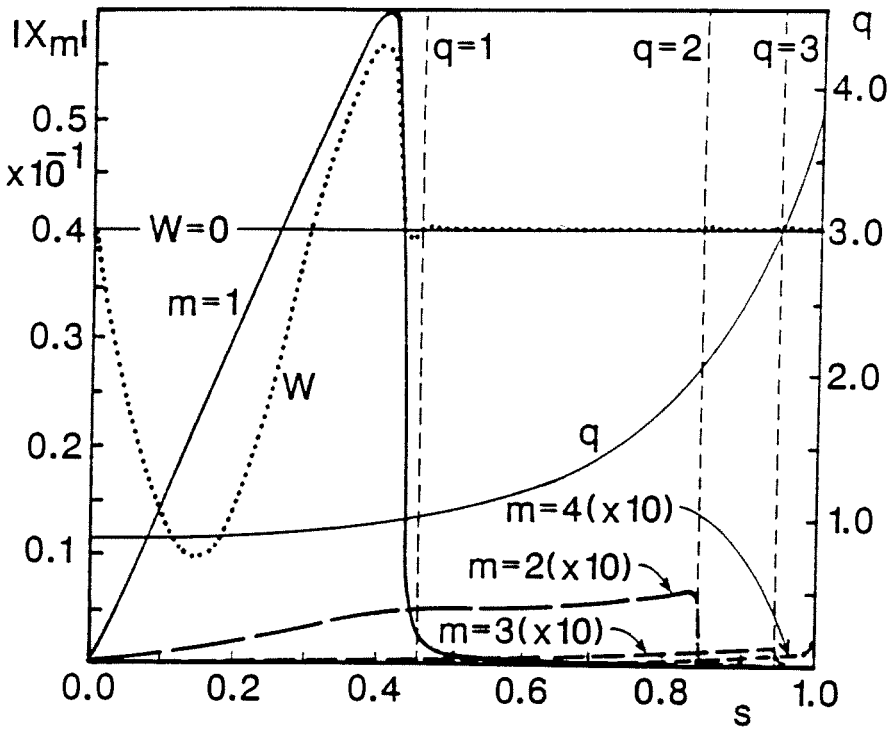

Turnbull
CRPP
Fig. 5c

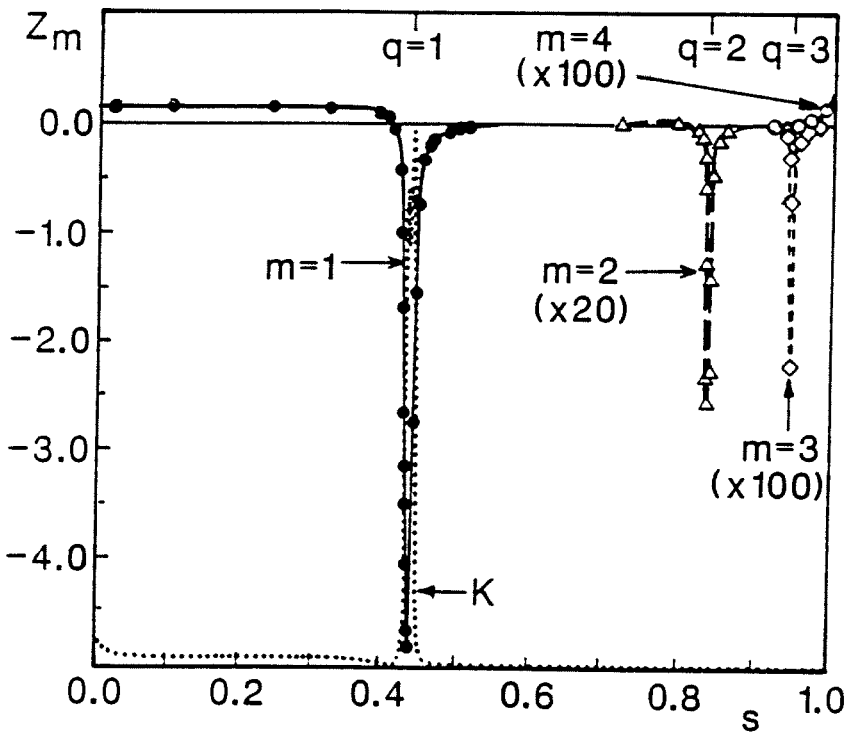

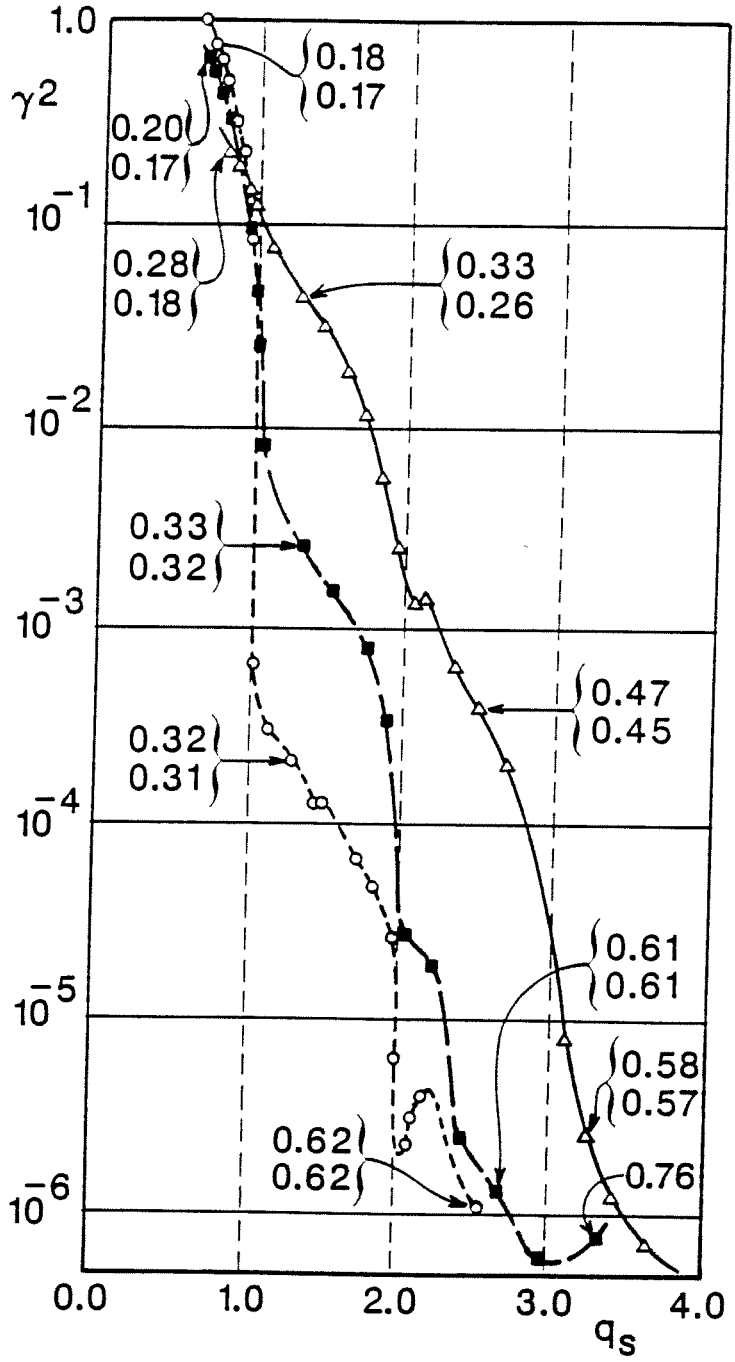
1.0
γ2
10−1
10−2
10−3
10−4
10−5
10−6
0.0
1.0
2.0
3.0
4.0
qs
0.18
0.17
0.20
0.17
0.28
0.18
0.33
0.26
0.33
0.32
0.47
0.45
0.32
0.31
0.61
0.61
0.58
0.57
0.62
0.62
0.76

Turnbull
CRPP
Fig. 7a

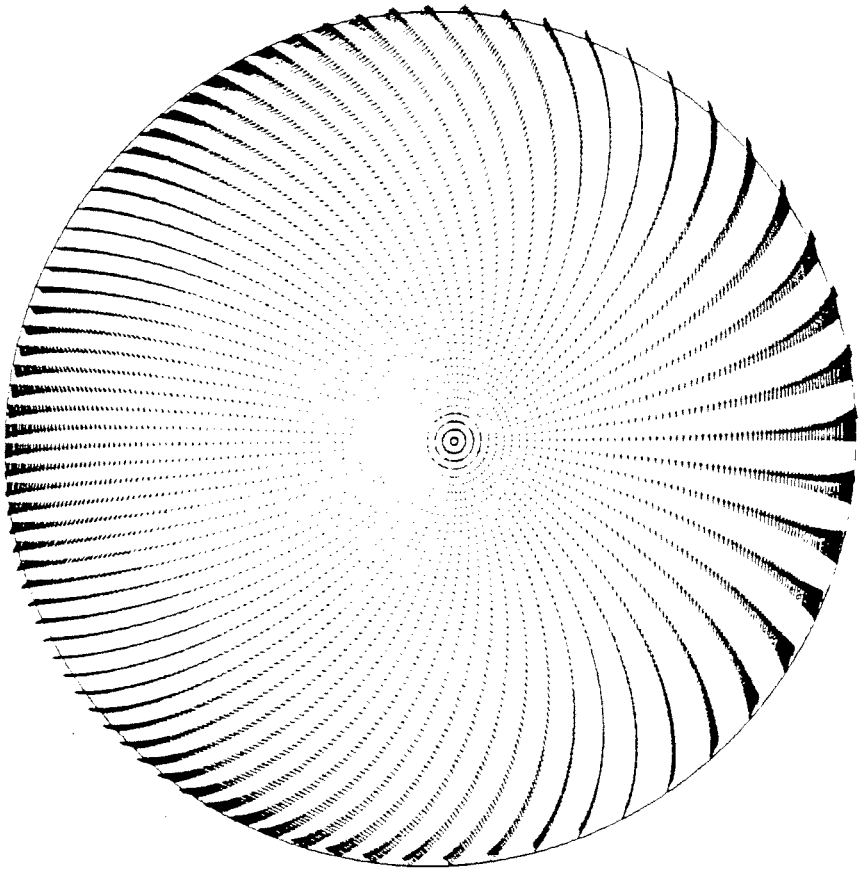

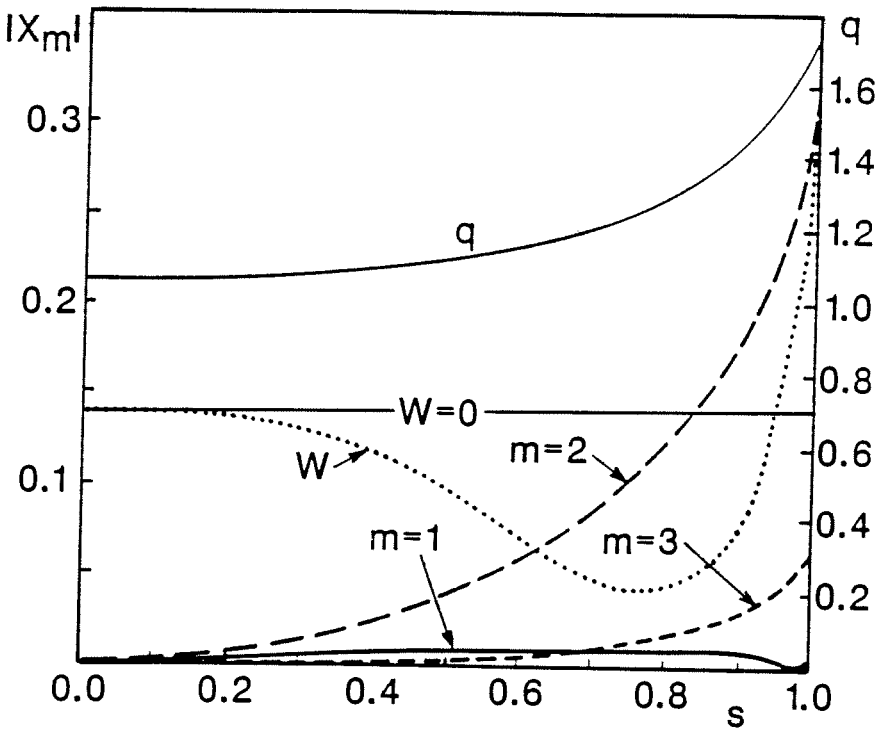
|Xm|
q
0.3
0.2
0.1
1.6
1.4
1.2
1.0
0.8
0.6
0.4
0.2
q
W=0
W
m=2
m=1
m=3
0.0
0.2
0.4
0.6
0.8
1.0
s

Turnbull
CRPP
Fig. 8a

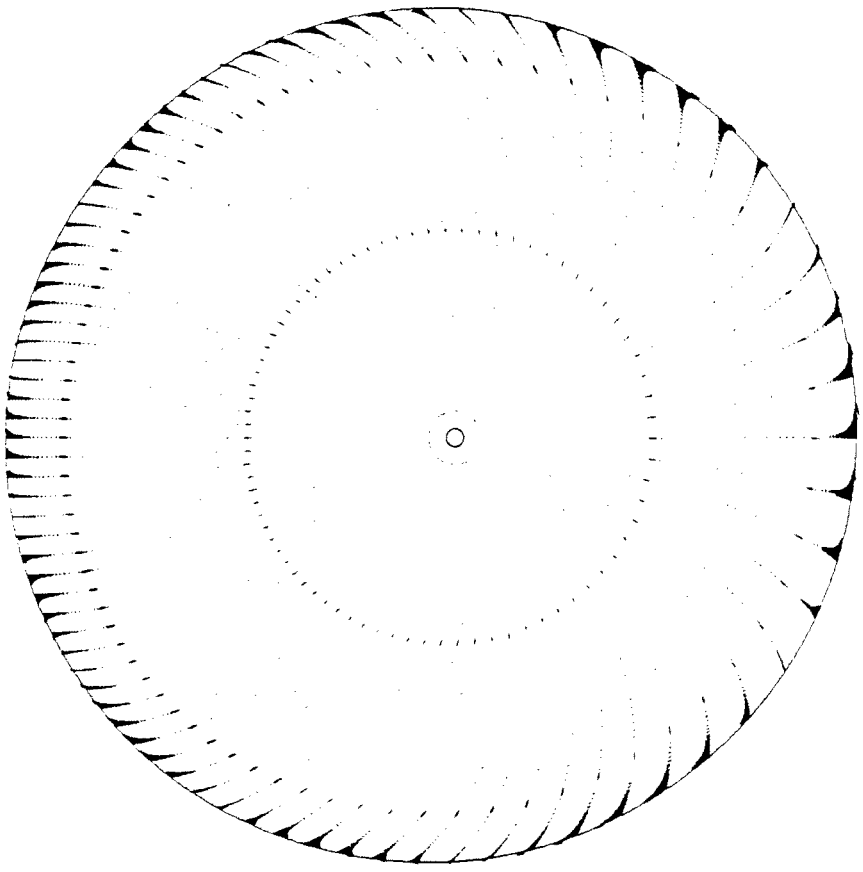

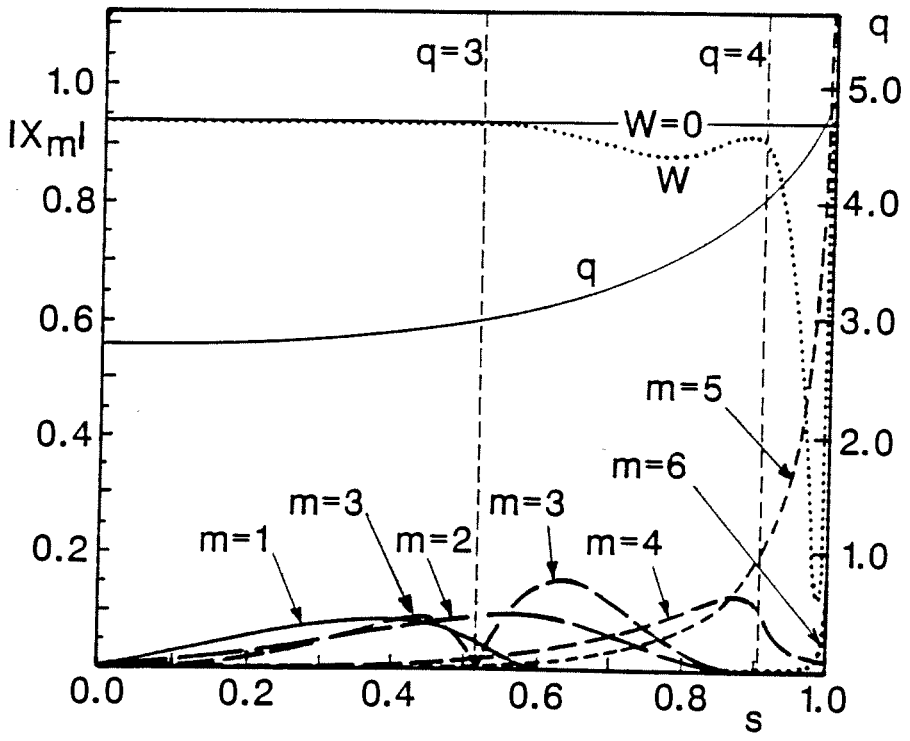
q=3
q=4
q
1.0
|Xm|
W=0
W
5.0
0.8
4.0
q
0.6
3.0
m=5
0.4
2.0
m=6
m=3
m=3
m=1
m=2
m=4
0.2
1.0
0.0
0.2
0.4
0.6
0.8
1.0
s

Turnbull
CRPP
Fig. 9

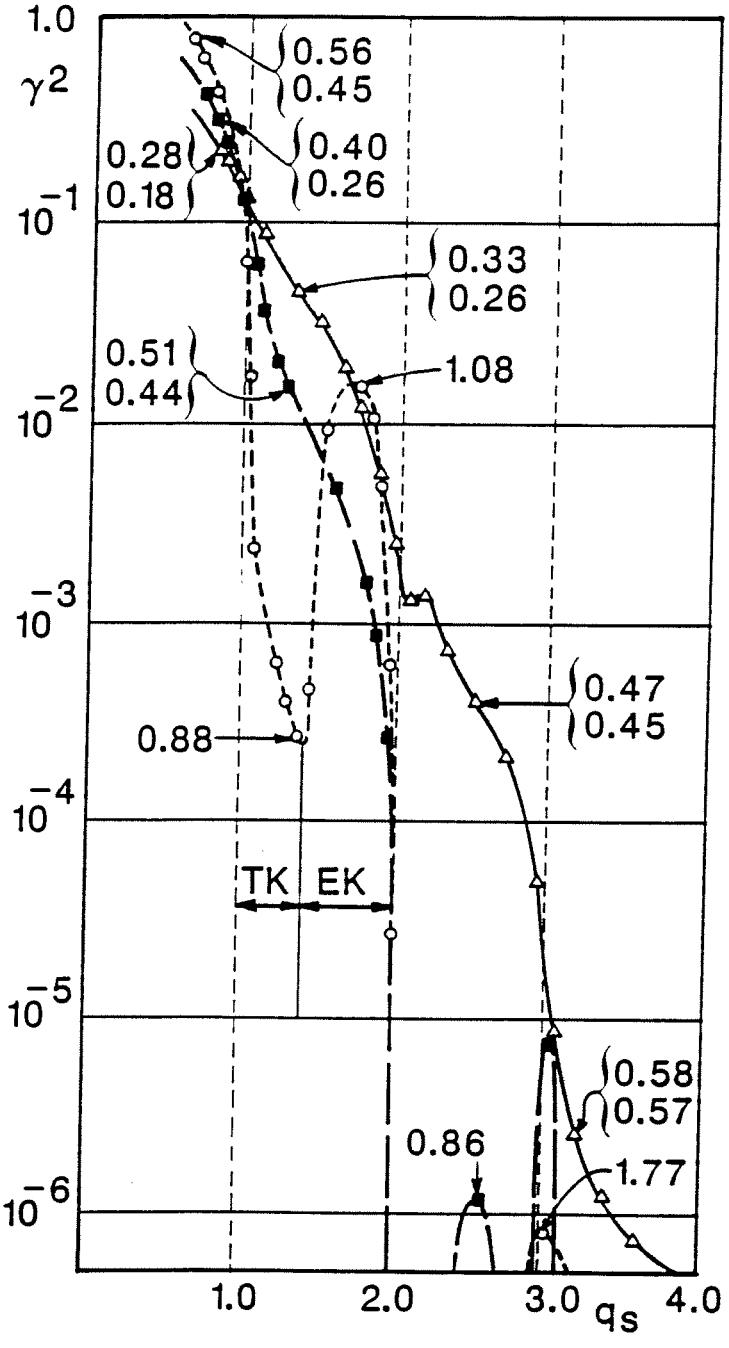

Turnbull
CRPP
Fig. 10a

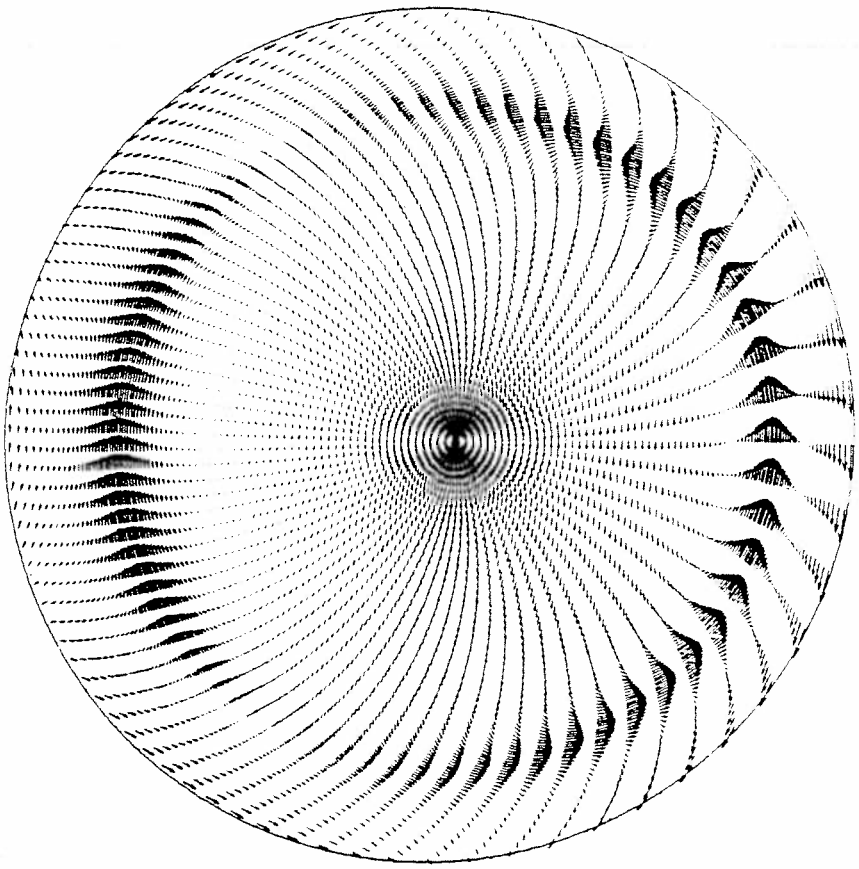

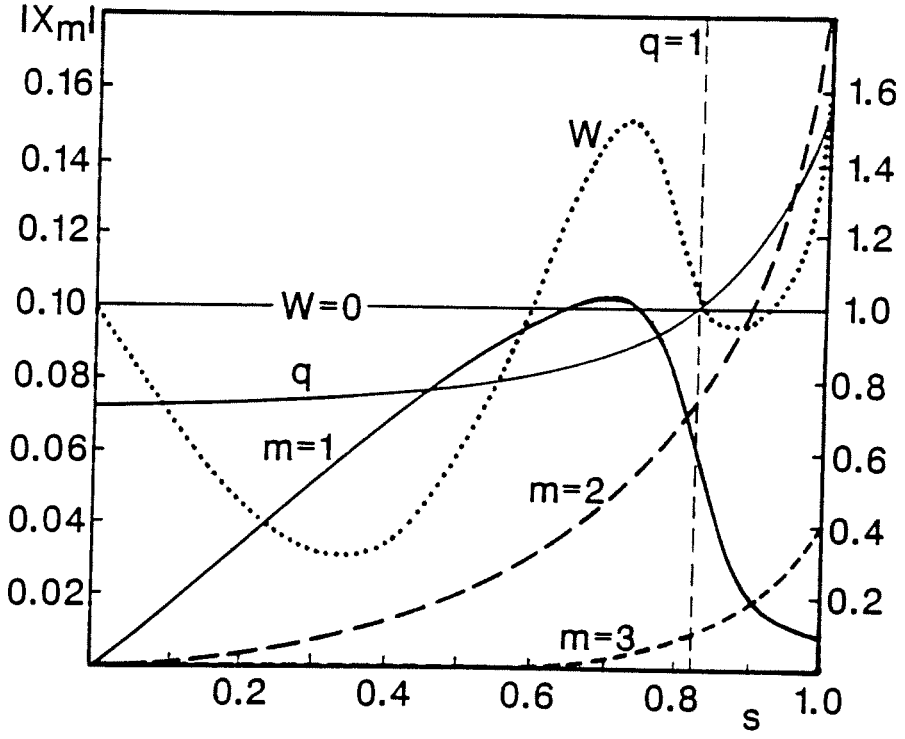
|Xm|
0.16
0.14
0.12
0.10
0.08
0.06
0.04
0.02
q=1
W
W=0
q
m=1
m=2
m=3
1.6
1.4
1.2
1.0
0.8
0.6
0.4
0.2
0.2
0.4
0.6
0.8
1.0
s

Turnbull
CRPP
Fig. 11a

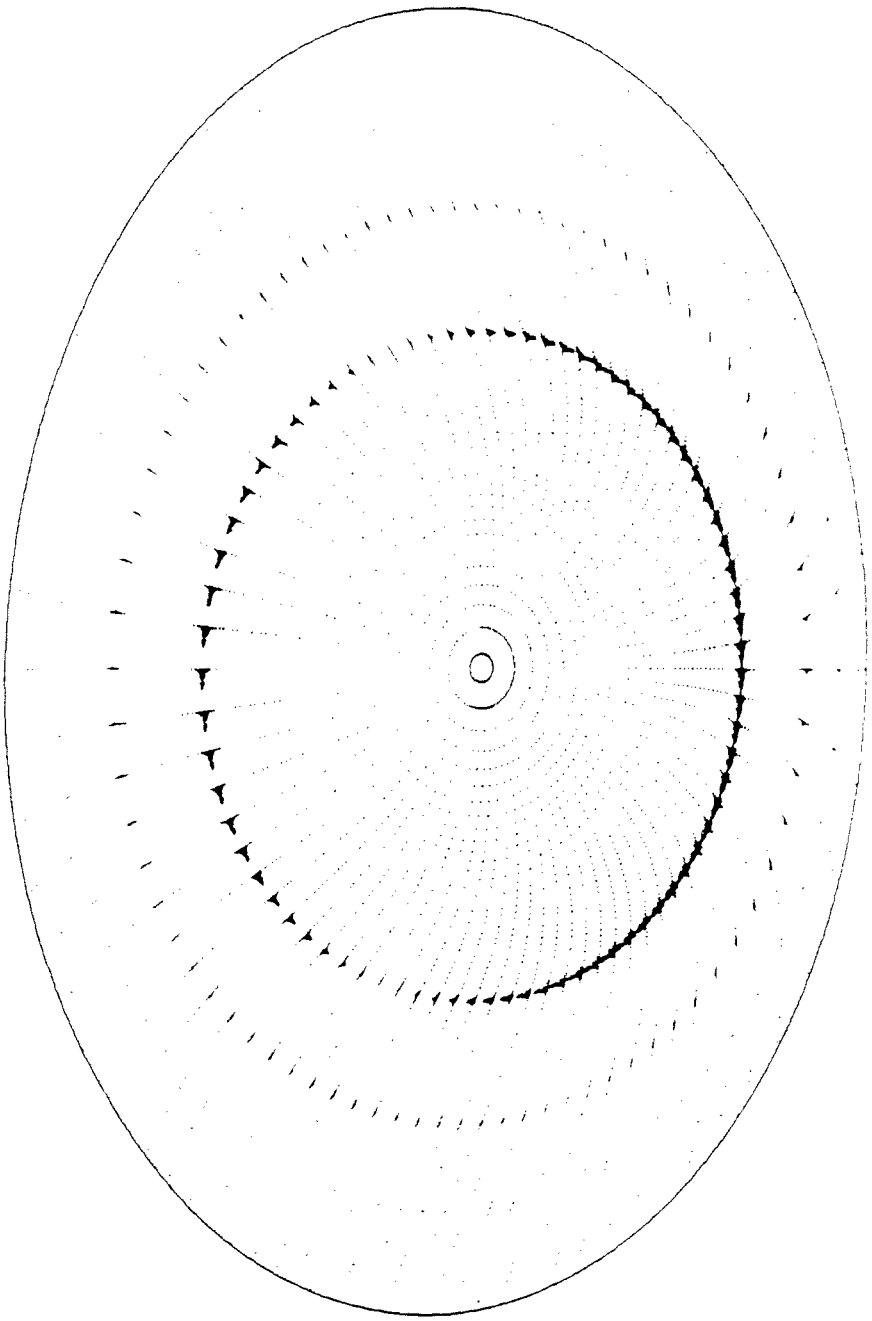

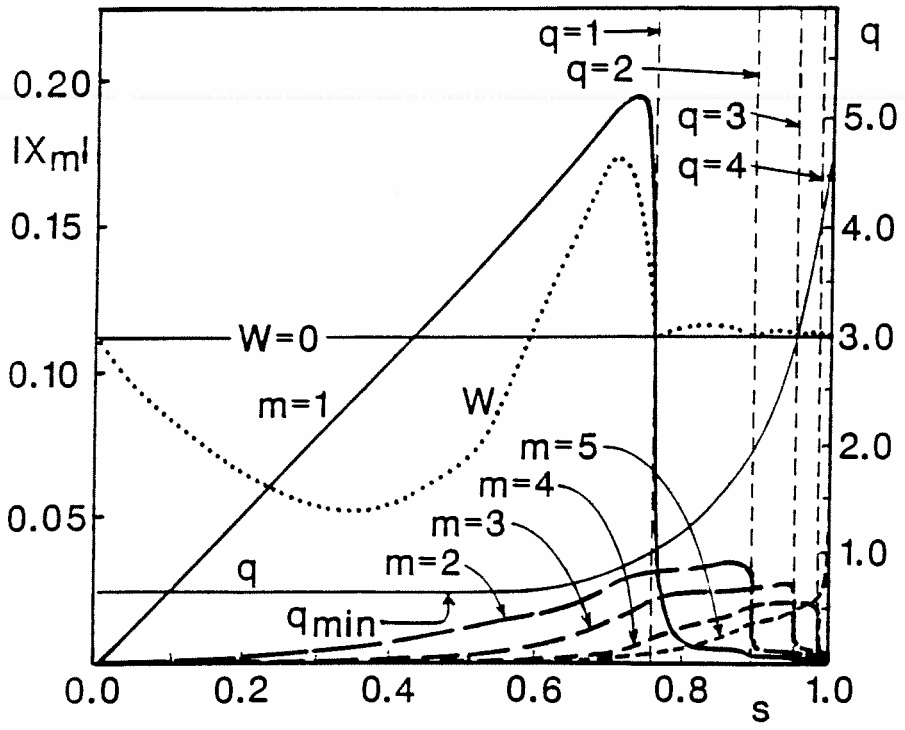
q=1
q=2
q=3
q=4
q
0.20
|Xm|
0.15
0.10
0.05
5.0
4.0
3.0
2.0
1.0
W=0
m=1
W
m=5
m=4
m=3
m=2
q
qmin
0.0
0.2
0.4
0.6
0.8
1.0
s